Optics and Laser Technology 119 (2019) 105662

Contents lists available at ScienceDirect

Optics and Laser Technology

journal homepage: www.elsevier.com/locate/optlastec

Full length article

Grain size evolution under different cooling rate in laser additive manufacturing of superalloy

Jiayun Shao[a,b], Gang Yu[a,b,c,*], Xiuli He[a,b,*], Shaoxia Li[a,b], Ru Chen[a,b], Yao Zhao[a,b]

[a] Institute of Mechanics, Chinese Academy of Sciences, Beijing 100190, China
[b] School of Engineering Science, University of Chinese Academy of Sciences, Beijing 100049, China
[c] Center of Materials Science and Optoelectronics Engineering, University of Chinese Academy of Sciences, Beijing 100049, China

HIGHLIGHTS

- Relationship between grain size, cooling rate and processing parameters had been studied.
- Arbitrary Lagrange-Euler method (ALE) was used to describe the free surface deformation.
- Solidification parameters especially cooling rate (G × R) were simulated to illustrate the underlying mechanisms.
- Grain size decreased with the increase of scanning speed due to the increase of cooling rate.
- A specific G-R map for the investigated Ni45 alloy in the region of equiaxed dendrite growth was obtained.

ARTICLE INFO

Keywords:
Laser additive manufacturing
Solidification
Grain size
Cooling rate
Superalloy

ABSTRACT

The processing parameters in laser additive manufacturing have a crucial impact on solidification microstructure especially grain size, thus influencing the properties of the final products. In this paper, experiments were conducted to investigate the effects of processing parameters including scanning speed, laser power and powder feeding rate on grain size of the solidified track during laser metal deposition. A three-dimensional model considering heat transfer, phase change and Marangoni convection flow had also been developed to simulate the solidification parameters especially cooling rate (G × R) to illustrate the underlying mechanisms. The experimental and simulated results indicated that cooling rate increased and grain size decreased from 8.7 μm to 4.7 μm with the increase of scanning speed from 2 mm/s to 10 mm/s. Contrarily, cooling rate decreased and grain size increased with the increase of laser power and powder feeding rate. The numerical and experimental results provide the additive manufacturing process with the potential of microstructure control and performance optimization.

1. Introduction

Additive manufacturing is based on a novel philosophy which is incrementally layer-by-layer manufacturing [1], contrary to conventional manufacturing techniques which are mostly based on the principle of material reduction. The concept of “Additive Manufacturing” (AM) offers the possibility of “Create Material” or “Design Material”. The idea of “Create Materials” by AM is a step-by-step process based on the ideas of “Use Materials” and “Develop Materials” which require integration of a tran-scale understanding of processing, microstructure and performance [2]. Laser additive manufacturing such as laser metal deposition (LMD), can coat, build and rebuild components having complex geometries, sound material integrity and dimensional accuracy [3]. LMD incorporated with the coaxially supplied powder feed stock has benefits such as small heat affected zone, low thermal strain, low porosity, fine grain size and high build rate [4]. During LMD, the laser heat source moves along with the feeding stock, leaving behind the solidified track. Complicated phenomena such as heat transfer, phase change, fluid flow are involved in this process [5]. There are many processing parameters such as laser power, scanning speed, powder feeding rate which influence this process. The complexity of these phenomena makes it difficult to select the proper combinations of processing parameters, in order to obtain desired microstructure and performance. A variety of alloys and metals have been used in laser additive manufacturing. Ni-based superalloys are typically used to manufacture hot-section components in chemical, aviation and

* Corresponding authors.
E-mail addresses: gyu@imech.ac.cn (G. Yu), xlhe@imech.ac.cn (X. He).

https://doi.org/10.1016/j.optlastec.2019.105662
Received 25 March 2019; Received in revised form 12 May 2019; Accepted 19 June 2019

aerospace industries [1], demanding excellent oxidation resistance and high strength at elevated temperatures which are closely related to grain size. With the refinement of grain size, the oxidation resistance increases and the strength in high temperature decreases. Thus, it is important to illustrate the relationship between processing parameters and consequential microstructure, especially grain size to design material with demanding performance.

Mesoscale understanding of laser additive manufacturing process can be provided by numerical modeling through study of phenomena such as heat transfer and fluid flow. Most of the research has focused on the temperature field, fluid field and the resultant molten pool shape [6–11]. Few models have been adopted to study the corresponding solidification parameters and its great potential to predict the subsequent microstructure. A three-dimensional finite element model [12] had been proposed to calculate the temperature gradient and solidification rate in the solid-liquid interface. The effect of substrate temperature and cooling rate on the particle distribution had been investigated by using a 3D transient heat transfer model [13]. A numerical model involving heat transfer, fluid flow and mass transfer [14] had been developed to study the thermal and solidification behavior in direct laser deposition. The effect of three-dimensional melt pool convection on temperature gradient and solidification growth velocity at the solidification front had been studied in Ref. [15]. Moreover, most of the numerical research focused on the effect of processing parameters on the grain morphology [16–20]. On the other hand, most of the experimental research has focused on the relationship between processing parameters and consequential grain morphology in laser additive manufacturing of nickel superalloy [21–24]. However, it is still challenging to predictably manipulate solidified grain structure, especially grain size and obtain desired microstructure by selecting processing parameters.

Grain size of solidified structure in laser additive manufacturing is strongly related to cooling rate, which is affected by many processing parameters like scanning speed, laser power and powder feeding rate. Moreover, it is hard to obtain cooling rate experimentally due to the intrinsic property of rapid solidification in laser additive manufacturing. In this study, analyses combining numerical modeling and experiments were conducted to study the relationship between processing parameters, cooling rate and grain size. A three-dimensional model was developed to study the solidification characteristics especially cooling rate ($G \times R$) under different processing parameters in LMD process with formation of a single track. Heat transfer, phase change and Marangoni convection flow were taken into consideration in this model. Meanwhile, experiments using Ni45 powder under different processing parameters including scanning speed, laser power and powder feeding rate were conducted to investigate the effect of processing parameters on grain size and the underlying mechanisms were revealed by the simulation.

2. Experiment procedure

The substrate and powder material were 1Cr13 stainless steel and Ni45 alloy powder, respectively. The chemical composition of 1Cr13 stainless steel and Ni45 alloy powder particle is shown in Table 1. Fig. 1(a) shows the morphology of Ni45 powder particle taken by ZEISS EVO18 scanning electron microscope (SEM), which was mostly spherical. Fig. 1(b) shows the size distribution of powder particle which was measured by sieve analysis and the Rosin-Rammler approximation. The range of powder particle diameter was 45–125 μm and the median diameter of powder particle was 91 μm.

Table 1
Chemical composition of 1Cr13 stainless steel and Ni45 powder (wt%).

	Fe	Cr	C	Si	Ni
1Cr13	Bal	12.0	0.1	0.8	0.6
Ni45	17.0	14.0	0.4	3	Bal.

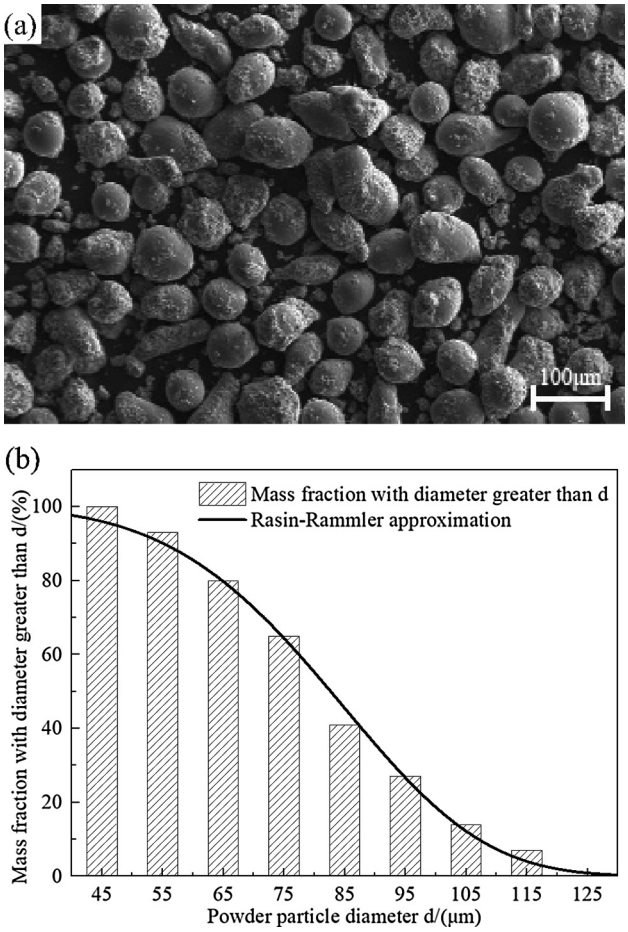

Fig. 1. (a) The SEM image of Ni45 powder particle and (b) the powder particle size distribution.

An Nd: YAG laser with a maximum power of 1000 W, a 1.06 μm wavelength and a 160 mm focal length was used as the heat source. The pattern of laser beam was multi-mode and the beam radius was set as 1 mm. The powder was fed coaxially and protected by highly purified argon shielding gas. The processing parameters are listed in Table 2 and six experiments were performed while the interval of scanning speed, laser power and powder feeding rate was 4 mm/s, 200 W and 1 g/min, respectively. Metallographic samples were cut, mounted, milled, polished, and etched in aqua regia solution sequentially. The solidified structure was observed by POLYVAR optical microscopy (OM) and ZEISS EVO18 scanning electron microscope (SEM). The grain size was measured via Nano Measurer software.

3. Numerical model

Fig. 2 shows a schematic diagram of a coaxial LMD process. The powder particles are injected into the molten pool coaxially with the help of inert gas and immediately melted under the heating of laser beam. The coaxial nozzle moves along with the laser beam at the predefined scanning speed. After the moving of laser source, rapid

Table 2
Processing parameters used in experiments for LMD.

Laser power (W)	Scanning speed (mm/s)	Powder feeding rate (g/min)
700–900	2–10	3–5

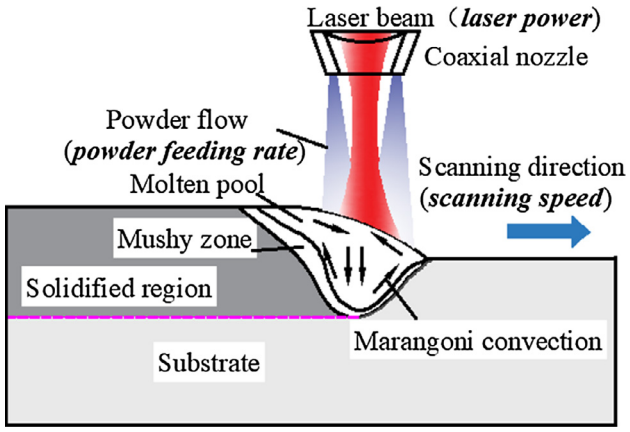

Fig. 2. A schematic diagram of the coaxial LMD process.

Table 3
Data used in calculations.

Parameters	Value	References
Laser spot radius r_b (mm)	1	–
Absorptivity of laser energy η_l	0.45	[32]
Powder flow radius r_p(mm)	2.5	–
Powder catchment efficiency η_m	0.9	–
Convective heat transfer coefficient h_c (W m^{-2} K^{-1})	100	[11]
Stefan-Boltzmann constant σ_b (W m^{-2} K^{-4})	5.67×10^{-8}	–
Emissivity ε	0.7	[33]
Ambient temperature T_0(K)	293.15	–

Table 4
Thermophysical properties of the material.

Properties	Value	References
Solidus temperature T_s (K)	1533	[34]
Liquidus temperature T_l (K)	1613	[34]
Solid density ρ_s (kg m^{-3})	8230	[34]
Liquid density ρ_l (kg m^{-3})	7130	[34]
Solid thermal conductivity k_s (W m^{-1} K^{-1})	33	[34]
Liquid thermal conductivity k_l (W m^{-1} K^{-1})	35	[34]
Solid specific heat c_{ps} (J kg^{-1} K^{-1})	473	[34]
Liquid specific heat c_{pl} (J kg^{-1} K^{-1})	540	[34]
Latent heat of fusion L (kJ kg^{-1} K^{-1})	273	[34]
Dynamic viscosity μ (Pa s)	5×10^{-3}	[11]
Surface tension σ_0 (N m^{-1})	1.943	[35]
Constant A (N m^{-1} K^{-1})	4.3×10^{-4}	[35]
Universal gas constant R (J kmol^{-1} K^{-1})	8314	[35]
Surface excess Γ_s (K mol m^{-2})	1.3×10^{-8}	[35]
Active element activity α_s (%)	0.03	–
Enthalpy ΔH_0 (kJ kmol^{-1})	-1.66×10^{-8}	[35]
Constant k	0.00318	[35]

solidification of melted alloy occurs and deposited layer forms over the substrate. A three-dimensional model considering heat transfer, phase change and Marangoni convection flow has been developed, correspondingly. Some simplifying assumptions in the model are listed as follows:

1. The material is isotropic and homogeneous. The thermophysical properties of substrate and powder are considered as the same and temperature-independent.
2. The mushy zone is assumed to be isotropic porous media.
3. The fluid flow in the melt pool is Laminar, Newtonian and incompressible.
4. The distribution of energy and powder flow is assumed to be Gaussian.
5. The heat loss by evaporation and the energy attenuation of laser beam through the powder flow are neglected. The heat flux of the heated powder is also neglected.

3.1. Governing equations

For the sake of computational source, the governing equations for the mass, momentum, and energy conservation are solved in half of the domain in the present model. The governing equations are listed below.

3.1.1. Mass conservation

The mass conservation equation is written as

$$\nabla \cdot \vec{u} = 0 \tag{1}$$

3.1.2. Momentum conservation

The momentum conservation equation is written as

$$\rho \frac{\partial \vec{u}}{\partial t} + (\rho \vec{u} \cdot \nabla)\vec{u} = -\nabla p + \nabla \cdot (\mu(\nabla \vec{u} + (\nabla \vec{u})^T)) - C\frac{(1-f_l)^2}{B+f_l^3}\vec{u} \tag{2}$$

where $\vec{u}$ is the velocity vector of the liquid metal, ρ, t, p and μ represent the density defined in Eq. (5), time, pressure and dynamic viscosity, respectively. The last term of Eq. (2) represents the momentum dissipation in the mushy zone depending on the Kozeny-Carman equation for flow through the porous media [25–26]. C is a constant depending on the morphology of the mushy zone (10^6 in this study). B is a small number to avoid division by zero (10^{-3} in this study). The liquid fraction f_l depending on solidus temperature (T_s) and liquidus temperature (T_l) is given by Eq. (3).

$$f_l = \begin{cases} 0 & T < T_s \\ \frac{T-T_s}{T_l-T_s} & T_s \leqslant T \leqslant T_l \\ 1 & T > T_l \end{cases} \tag{3}$$

3.1.3. Energy conservation

Due to the existence of solid-liquid phase change, the latent heat is included in the energy conservation. The energy conservation equation is written as

$$\rho c_p \frac{\partial T}{\partial t} + \rho c_p \vec{u} \cdot \nabla T = \nabla \cdot (k \nabla T) - \frac{\partial H}{\partial t} - \rho \vec{u} \cdot \nabla H \tag{4}$$

where ρ, c_p and k are the density, specific heat and thermal conductivity which are defined as [27]

$$\rho = (1-f_l)\rho_s + f_l \rho_l \tag{5}$$

$$c_p = (1-f_l)c_{ps} + f_l c_{pl} \tag{6}$$

$$k = (1-f_l)k_s + f_l k_l \tag{7}$$

H is the latent enthalpy of the fusion which is defined as

$$\Delta H = L f_l \tag{8}$$

where L is the latent heat.

In Eqs. (5)–(8), the subscript s and l represent the solid and liquid phase, respectively.

3.2. Arbitrary Lagrange-Euler method (ALE)

The free surface deformation is described by ALE [28]. Two types of velocities are taken into account at liquid/gas interface – the fluid flow velocity and the boundary moving velocity due to mass addition [29]. Thus, the velocity at the liquid/gas interface $V_{L/G}$ can be given as

$$V_{L/G} = \vec{u} \cdot \vec{n} + \vec{V}_p \cdot \vec{n} \tag{9}$$

where $\vec{u}$ is the velocity of the fluid flow at liquid/gas interface and $\vec{n}$ is the normal vector of the interface. $\vec{V}_p$ is the moving velocity at the

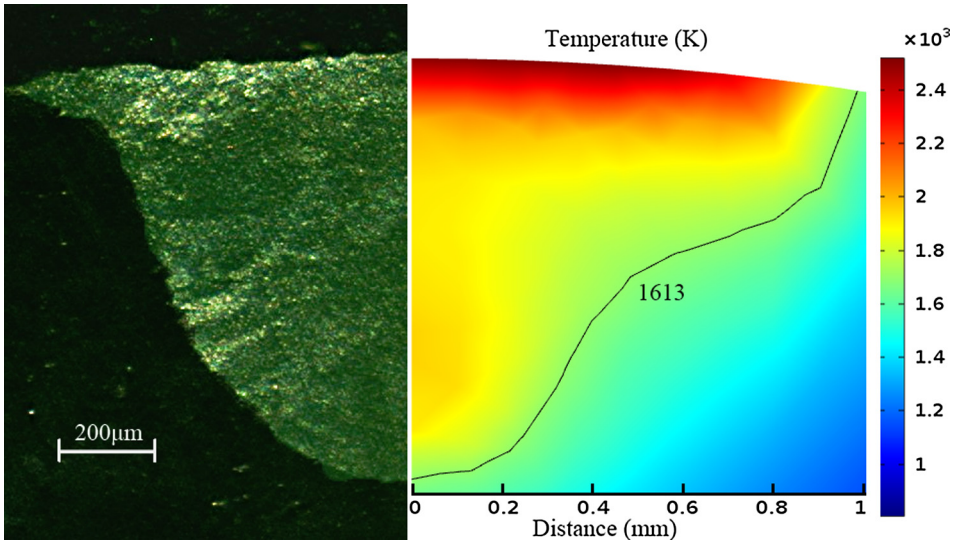

Fig. 3. Experimental and simulated molten pool in the transverse section.

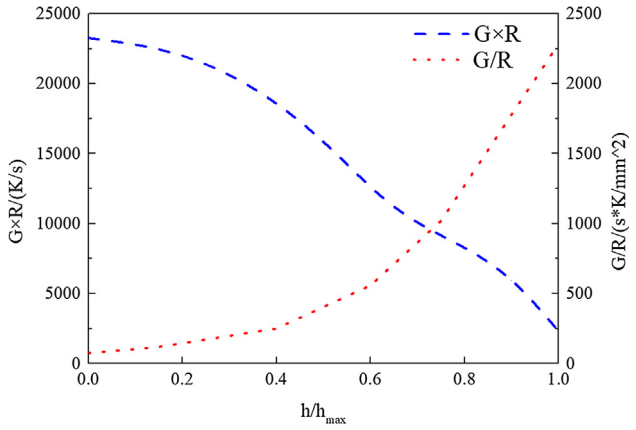

Fig. 4. Simulated cooling rate (G × R) and G/R in the transverse section.

interface because of mass condition, which is defined as

$$\vec{V_p} = \frac{2m_f\eta_m}{\rho_m \pi {r_p}^2} exp\left(\frac{-2((x - V_s t)^2 + y^2)}{{r_p}^2}\right)\vec{z} \tag{10}$$

where m_f is the powder flow rate, η_m, ρ_m, r_p and V_s represent the powder catchment efficiency, density of powder, powder flow radius and scanning speed, respectively. In addition, x and y are the distances to the laser beam and $\vec{z}$ is the unit vector in the z direction.

3.3. Boundary conditions

An equation considering the laser heat flux and the heat loss by convection and radiation is given as

$$q_{in} = \frac{2Q\eta_l}{\pi {r_b}^2} exp\left(\frac{-2((x - V_s t)^2 + y^2)}{{r_b}^2}\right) - h_c(T - T_0) - \sigma_b \varepsilon (T^4 - T_0^4) \tag{11}$$

where Q, η_l, r_b, h_c, σ_b and ε represent the laser power, absorptivity of laser energy, effective laser beam radius, convective heat transfer coefficient, Stefan-Boltzmann constant and emissivity, respectively.T_0 is the ambient temperature.

At the liquid/gas interface, the boundary condition of momentum equation is given as

$$F_{L/G} = \sigma\kappa\vec{n} - \nabla_s T\frac{d\sigma}{dT} \tag{12}$$

where κ is the curvature of surface. σ is the surface tension, given as Eq. (13). The first term of Eq. (12) is capillary force and second term is thermocapillary force.

$$\sigma = \sigma_0 + \frac{d\sigma}{dT}(T - T_s) \tag{13}$$

where $\sigma_0$is the surface tension of the pure metal at a reference temperature and $\frac{d\sigma}{dT}$ is the temperature coefficient of surface tension. Considering the effect of active element, $\frac{d\sigma}{dT}$ is given as [30]

$$\frac{d\sigma}{dT} = -A - R\Gamma_s ln(1 + K\alpha_s) - \frac{K\alpha_s\Gamma_s\Delta H_0}{T(1 + K\alpha_s)} \tag{14}$$

where A, R, Γ_s, α_s and ΔH_0 are the constant which expresses the variation of surface tension of pure metal at temperature above the melting point, the universal gas constant, the surface excess in saturation, the activity of active element (which is sulfur in this paper) in the alloy and the enthalpy of segregation, respectively. K is the entropy factor which is given as

$$K = k_l \exp\left(-\frac{\Delta H_0}{RT}\right) \tag{15}$$

where k_l is a constant corresponding to the segregation entropy.

Other surfaces of the computational domain are considered as insulation except for the symmetric plane.

3.4. Solidification parameters

Temperature gradient normal to the liquid-solid interface G and solidification velocity of the liquid-solid interface R are two key parameters of solidification characteristics [31], which are defined as

$$G = \nabla T \cdot \vec{n_0} \tag{16}$$

$$R = V_s \cdot \vec{i} \cdot \vec{n_0} \tag{17}$$

where $\vec{n_0}$ is the unit normal vector of the solidification front and $\vec{i}$ is the unit vector of the scanning direction. V_s is the scanning speed. Furthermore, cooling rate G × R and G/R are two key solidification parameters while G × R is one of the most important variables in determining grain size and G/R is important in determining grain morphology [31].

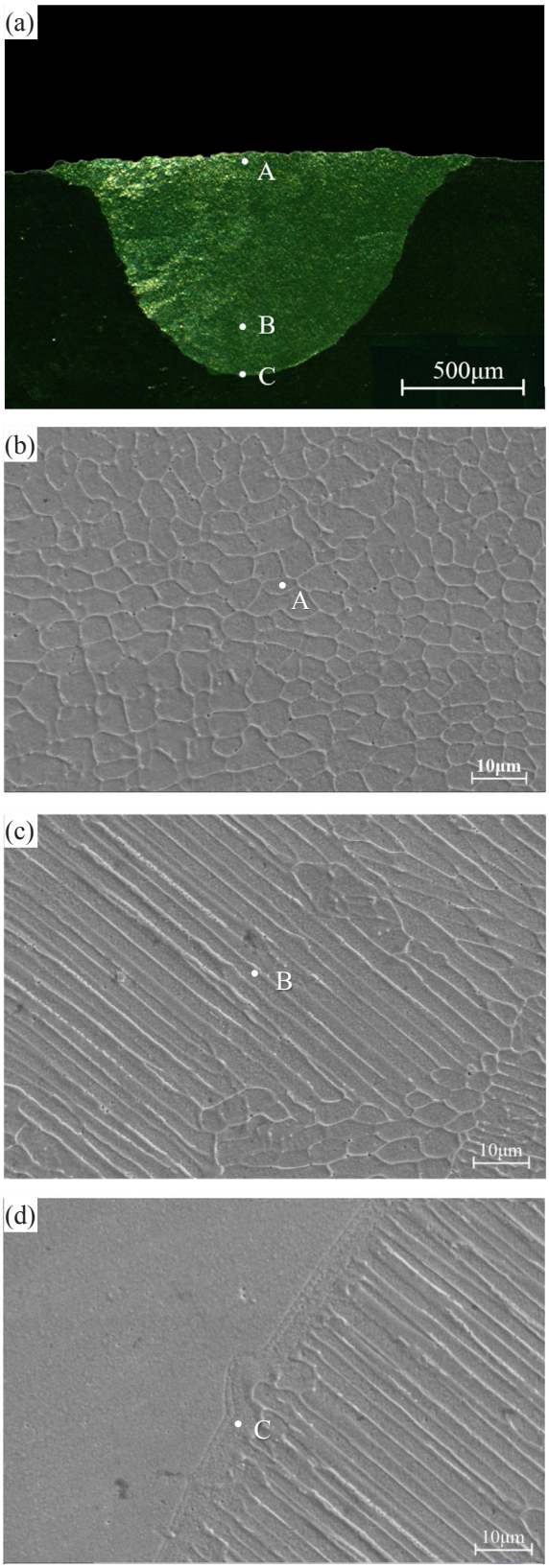

Fig. 5. Experimental transverse section of (a) deposited track and microstructure in the point of (b) A, (c) B and (d) C.

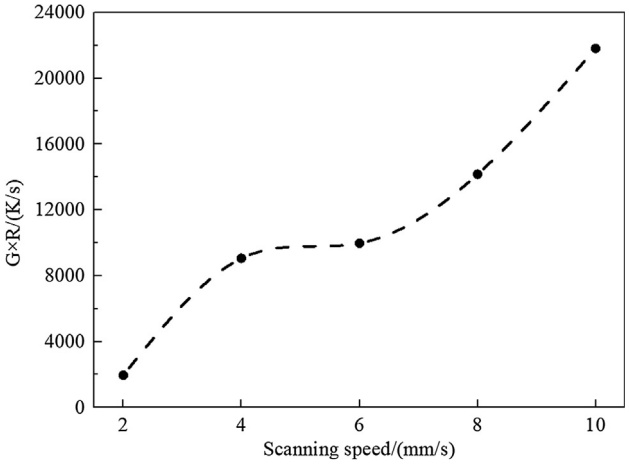

Fig. 6. Simulated cooling rate (G × R) at different scanning speed.

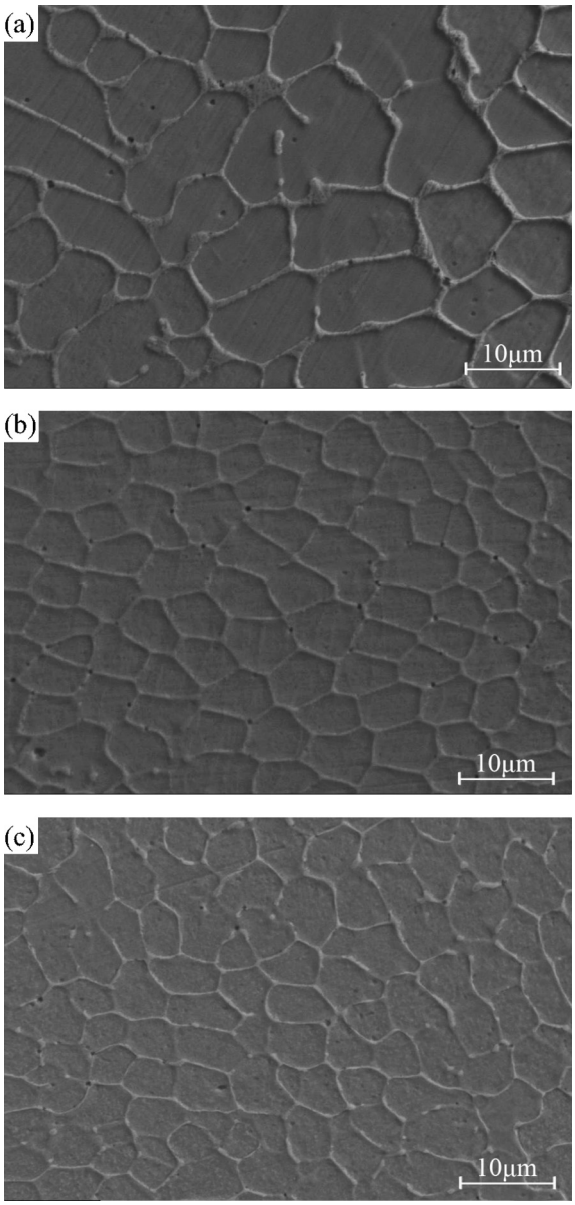

Fig. 7. Experimental equiaxed dendrites at scanning speed of (a) 2 mm/s, (b) 6 mm/s and (c) 10 mm/s.

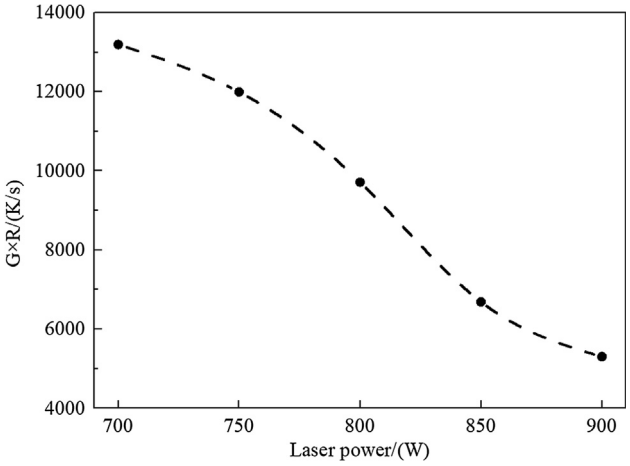

Fig. 8. Simulated cooling rate (G × R) at different laser power.

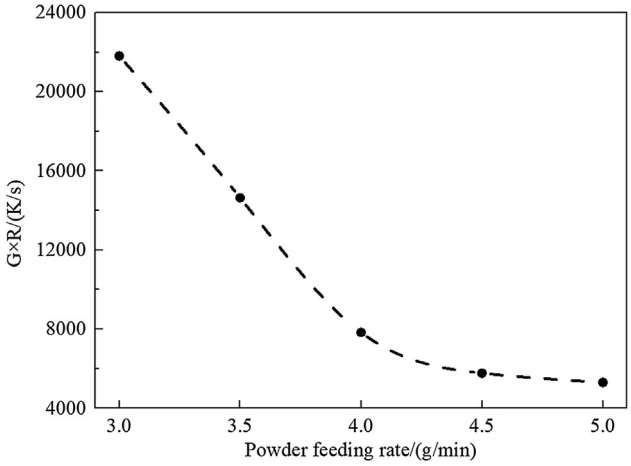

Fig. 10. Simulated cooling rate (G × R) at different powder feeding rate.

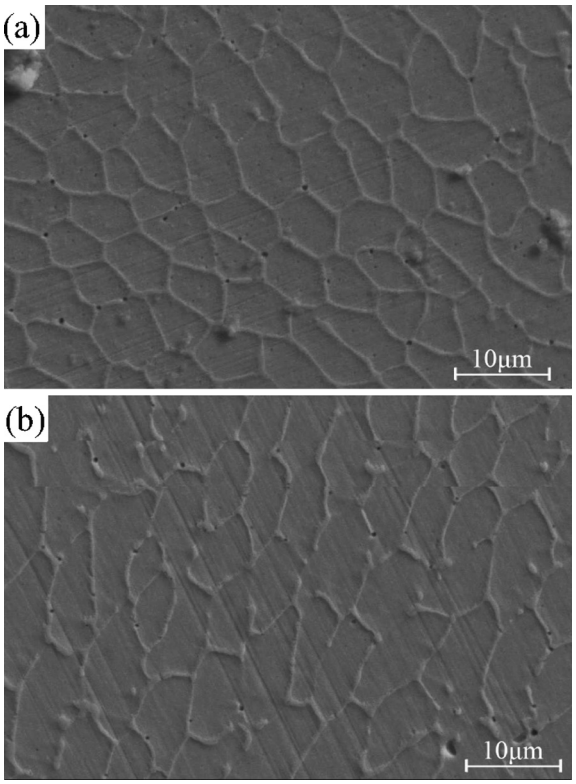

Fig. 9. Experimental equiaxed dendrites at laser power of (a) 700 W and (b) 900 W.

3.5. Parameters used in simulations

The processing parameters used for the modeling are listed in Table 3. The laser power used in the model ranges from 700 W to 900 W. The scanning speed ranges from 2 mm/s to 10 mm/s and the powder feeding rate ranges from 3 g/min to 5 g/min. The thermo-physical properties of the material are listed in Table 4.

4. Results

4.1. Solidification characteristics

The change of solidification parameters and microstructure including solidified morphology and grain size were investigated first while scanning speed was 10 mm/s, laser power was 900 W and powder

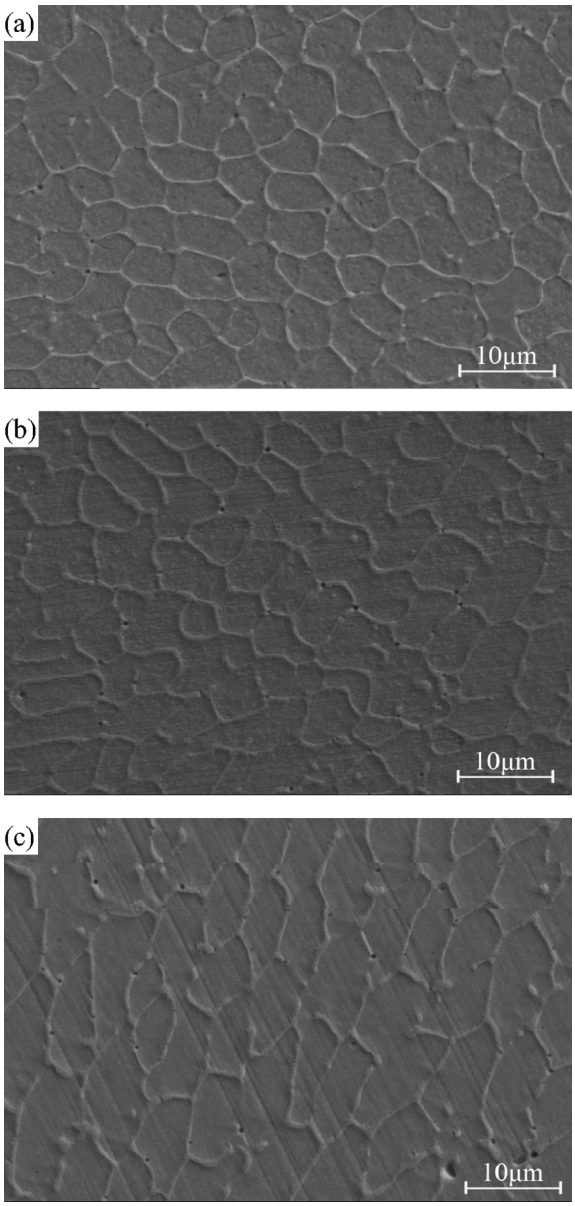

Fig. 11. Experimental equiaxed dendrites at powder feeding rate of (a) 3 g/min, (b) 4 g/min and (c) 5 g/min.

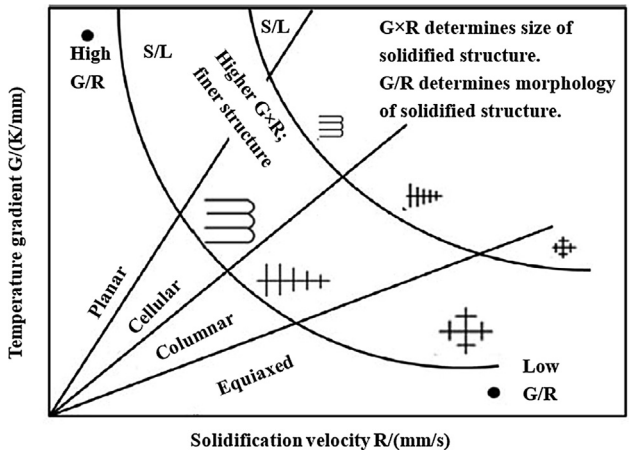

Fig. 12. The effects of G and R on the morphology and the scale of the solidified structure [31]

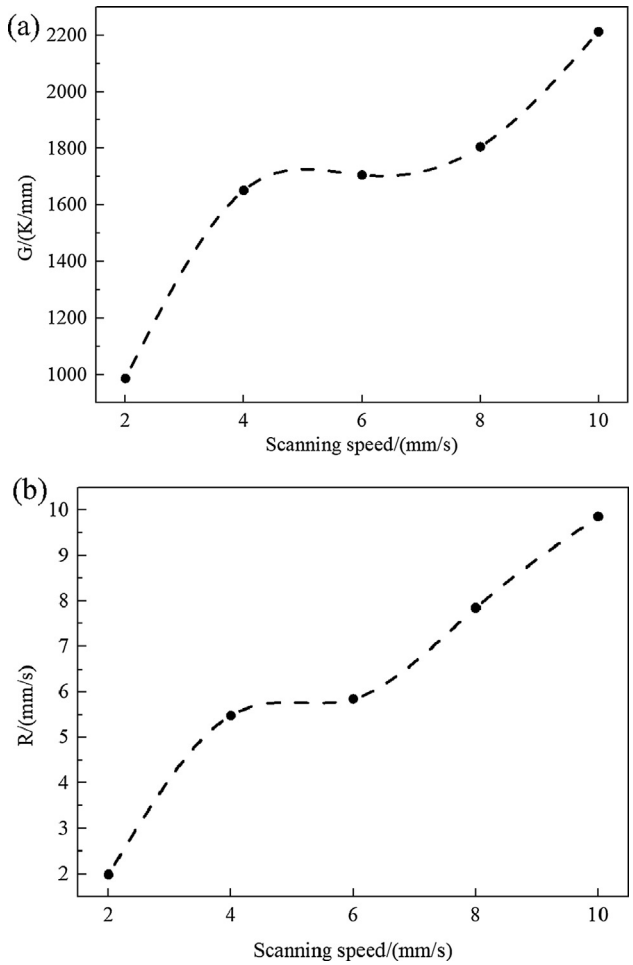

Fig. 13. Simulated (a) temperature gradient (G) and (b) solidification velocity at liquid-solid interface (R) at different scanning speed while laser power was 900 W and powder feeding rate was 3 g/min.

feeding rate was 3 g/min. Fig. 3 shows the simulated and experimental molten pool in the transverse section. The good agreement between experimental and numerical results has indicated the validity of the model. Fig. 4 shows the change of solidification parameters cooling rate (G × R) and G/R in the transverse section with the ratio of height to molten pool depth. As shown in Fig. 4, G/R increased from 74 to 2285 s * K/mm^2 and G × R decreased from 23,263 to 2309 K/s from the top to the bottom of the molten pool. Fig. 5 shows the experimental transverse section of deposited track and the microstructure in the point of A, B and C, which were located in the upper, the central and the bottom cross-section, respectively. Fig. 5(b), (c) and (d) represented equiaxed dendrites, columnar dendrites and planar front, respectively. From the top to the bottom of the deposited layer, the solidified morphology changed from equiaxed dendrites, columnar dendrites to planar front.

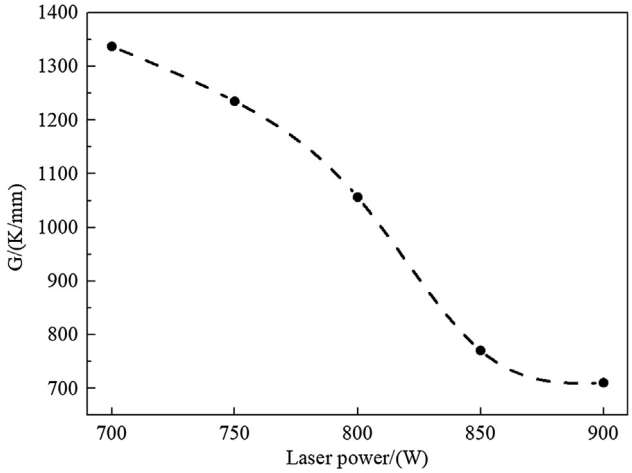

Fig. 14. Simulated temperature gradient (G) at different laser power while scanning speed was 10 mm/s and powder feeding rate was 5 g/min.

Table 5
Simulated solidification velocity at the liquid-solid interface (R) at different laser power while scanning speed was 10 mm/s and powder feeding rate was 5 g/min.

Laser power/W	700	750	800	850	900
Solidification velocity R/(mm/s)	9.8	9.7	9.2	8.7	7.4

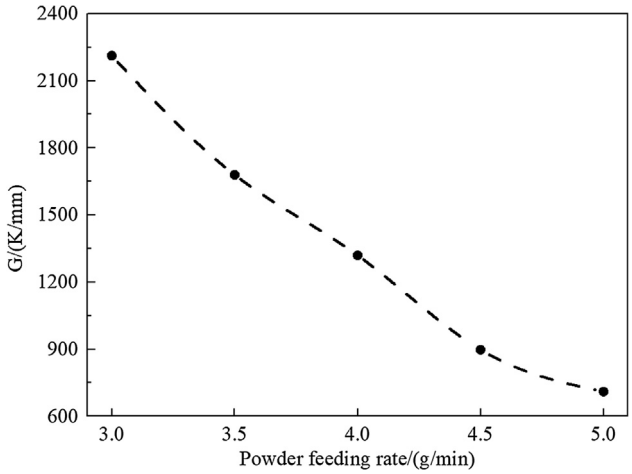

Fig. 15. Simulated temperature gradient (G) at different powder feeding rate while scanning speed was 10 mm/s and laser power was 900 W.

Table 6
Simulated solidification velocity at the liquid-solid interface (R) at different powder feeding rate while laser power was 900 W and scanning speed was 10 mm/s.

Powder feeding rate/(g/min)	3	3.5	4	4.5	5
Solidification velocity R/(mm/s)	9.6	8.7	8.3	6.1	7.2

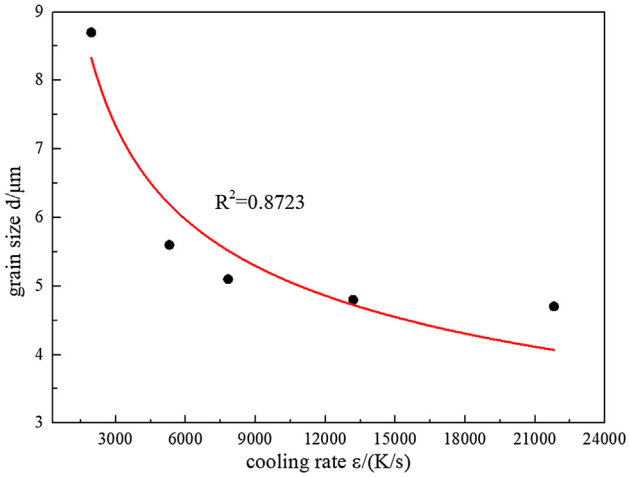

Fig. 16. The grain size under different cooling rate.

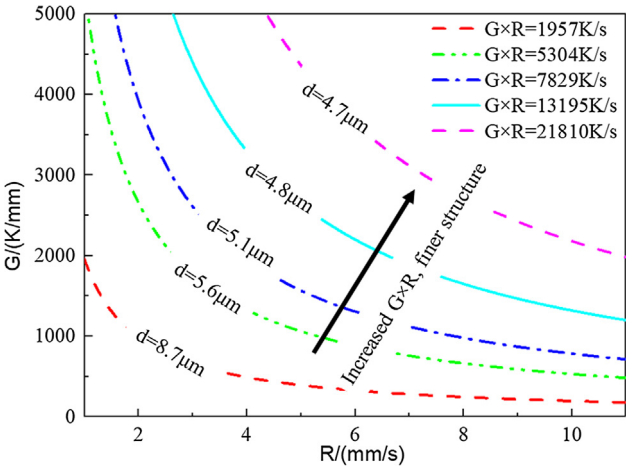

Fig. 17. The specific G-R map to the investigated Ni45 alloy in the region of equiaxed dendrite growth.

4.2. Effects of scanning speed

For the sake of comparison, all the equiaxed dendrites were taken at almost the same ratio of deposited layer depth correspondingly, which means the equiaxed dendrites were taken near the top (such as point A in Fig. 5(a)) of the deposited layer. Fig. 6 shows the simulated cooling rate (G × R) at different scanning speed while the laser power was 900 W and the powder feeding rate was 3 g/min. As shown in Fig. 6, with the increase of scanning speed from 2 mm/s to 10 mm/s, G × R increased from 1957 to 21810 K/s. Fig. 7 shows the equiaxed dendrites at different scanning speed. As shown in Fig. 7, the average size of equiaxed dendrites was 8.7 μm, 5.4 μm and 4.7 μm at the scanning speed of 2 mm/s, 6 mm/s and 10 mm/s, respectively. With the increase of scanning speed, the average size of equiaxed dendrites decreased.

4.3. Effects of laser power

Fig. 8 shows the simulated cooling rate (G × R) at different laser power while the scanning speed was 10 mm/s and the powder feeding rate was 5 g/min. As shown in Fig. 8, with the increase of laser power from 700 W to 900 W, G × R decreased from 13195 K/s to 5304 K/s. Fig. 9 shows the equiaxed dendrite at different laser power. As shown in Fig. 9, the average equiaxed dendrites size was 4.8 μm and 5.6 μm at laser power of 700 W and 900 W, respectively. With the increase of laser power, the average size of equiaxed dendrites slightly increased.

4.4. Effects of powder feeding rate

Fig. 10 shows the simulated cooling rate (G × R) at different powder feeding rate while the laser power was 900 W and the scanning speed was 10 mm/s. As shown in Fig. 10, with the increase of powder feeding rate from 3 g/min to 5 g/min, G × R decreased from 21810 K/s to 5304 K/s. Fig. 11 shows the equiaxed dendrites at different powder feeding rate. As shown in Fig. 11, the average size of equiaxed dendrites was 4.7 μm, 5.1 μm and 5.6 μm at the powder feeding rate of 3 g/min, 4 g/min and 5 g/min, respectively. With the increase of powder feeding rate, the average equiaxed dendrites size slightly increased from 4.7 μm to 5.6 μm.

5. Discussion

With the grain refinement, the oxidation resistance of superalloy is improved and the strength at high temperature is weaken [36,37]. Therefore, in order to achieve an optimal balance between oxidation resistance and high strength of superalloy at high temperature, appropriate processing parameters should be chosen to obtain desired grain size. Furthermore, as shown in Fig. 12, the solidification parameters cooling rate (G × R) and G/R are two key factors influencing the microstructure in rapid solidification, while G × R determines size of solidified structure and G/R determines morphology of solidified structure [31]. This paper studies the effects of processing parameters on grain size in laser additive manufacturing through experiments and reveals the mechanisms behind through numerical modeling.

As shown in Fig. 5(b), at the top of the molten pool where lower G/R and higher G × R were noticed, the morphology of the molten pool was equiaxed dendrite and the grain size was finer. As shown in Fig. 5(d), at the bottom of the molten pool where higher G/R were noticed, the morphology was planar front. As shown in Fig. 5(c), at the center of the molten pool where medium G/R was noticed, the morphology was columnar dendrites. As shown in Fig. 4 and Fig. 5, with G/R increasing from the top to the bottom of the molten pool, the solidified morphology changes from equiaxed dendrites, columnar dendrites to planar front.

Fig. 13 shows the simulated temperature gradient (G) and solidification velocity at liquid-solid interface (R) at different scanning speed. With the increase of scanning speed, both the temperature gradient and solidification velocity increased, causing the increase of cooling rate G × R (Fig. 6). As shown in Fig. 7, with the increase of G × R, the equiaxed dendrite was finer and the grain size decreased from 8.7 μm to 4.7 μm. These findings illustrate that with the increase of scanning speed, G and R increased, causing the increase of G × R and thus grain size decreased.

Fig. 14 shows the simulated temperature gradient (G) at different laser power. With the increase of laser power, more energy is absorbed in the molten pool, causing the increase of pool size, which causes the decrease of temperature gradient (G) due to the spreading of isotherms. On the other hand, as shown in Table 5, the solidification velocity (R) slightly decreased with the increase of laser power. Therefore, cooling rate (G × R) decreased with higher power. As shown in Fig. 8 and Fig. 9, with the increase of laser power from 700 W to 900 W, G × R decreased and the equiaxed dendrites were coarser, with the grain size slightly increasing from 4.8 μm to 5.6 μm. These findings illustrate that with the increase of laser power, G × R decreased and thus grain size slightly increased.

Fig. 15 shows the simulated temperature gradient (G) at different powder feeding rate. With the increase of powder feeding rates, G decreased. Moreover, the simulated solidification velocity (R), found in Table 6, didn't show monotonous change at different powder feeding rate. Therefore, with the increase of powder feeding rate, cooling rate (G × R) decreased mainly due to the decrease of temperature gradient. Furthermore, as shown in Fig. 10 and Fig. 11, with the increase of powder feeding rate from 3 g/min to 5 g/min, G × R decreased and the

equiaxed dendrites were coarsened, increasing from 4.7 μm to 5.6 μm. These findings illustrate that with the increase of powder feeding rate, G × R decreased and thus grain size slightly increased.

The grain size is primarily determined by the cooling rate G × R and the relationship between grain size and cooling rate can be described as [38]:

$$d = a(\varepsilon^{-n})$$

where d is the grain diameter (in μm), ε is the cooling rate (Ks^{-1}) which is presented by G × R in this paper; a and n are fitting factors. Fig. 16 shows the grain size under different cooling rate. The fitting equation was

$$d = 79 \cdot \varepsilon^{-0.3}$$

Fig. 12 shows a generic G-R map for solidification processing. Fig. 17 shows a specific G-R map for the investigated Ni45 alloy in the region of equiaxed dendrite growth according to the study. Since the transition of the solidified structure from planar front to columnar dendrites to equiaxed dendrites is not quantified in this study, the quantified results in Fig. 17 only represented the grain size evolution in the region of equiaxed dendrite growth and didn't illustrate the scale evolution of solidified structure in other regions. The quantified G-R map contributes to developing processing maps for selecting the appropriate processing parameters to achieve certain grain size and desired microstructure in Ni45 alloys.

The oxidation resistance and high-temperature strength of superalloys are closely related to the grain size. As the highly instable region compared with intragranular region, the grain boundary is the preferentially diffusive pathway which can accelerate the diffusion of selective oxidation components, helping to form protective oxide film. Thus, the oxidation resistance of superalloy increases with the grain refinement [36]. However, with the refinement of grain size, the grain boundary strength is weakened at high temperature due to the plastic deformation [37]. Thus, in order to choose proper combinations of processing parameters to acquire demanding performance for various applications, it is vital to investigate the relationship between processing parameters and grain size in laser additive manufacturing of superalloy. The selection explored by experiments is a trial and error technique which is time-consuming and money-consuming process caused by the numerous combinations. Besides, it is hard to measure the solidification parameters through experiments. Hence, this paper combining experiments and numerical modeling illustrates the relationship between processing parameters and microstructure especially grain size in laser metal deposition and interprets the mechanisms, moving forward to microstructure control and performance optimization for laser additive manufacturing.

6. Conclusion

Experimental and numerical studies have been conducted to study the relationship between cooling rate, grain size of solidified structure and processing parameters including scanning speed, laser power and powder feeding rate in laser metal deposition. With the increase of scanning speed from 2 mm/s to 10 mm/s, the temperature gradient(G) and solidification velocity at liquid–solid interface(R) increased, causing the increase of cooling rate (G × R) and the grain size decreased from 8.7 μm to 4.7 μm due to the increase of cooling rate. With the increase of laser power from 700 W to 900 W, temperature gradient decreased due to the spreading of isotherms. Cooling rate decreased mainly due to the decrease of temperature gradient and the grain size slightly increased, correspondingly. With the increase of powder feeding rate from 3 g/min to 5 g/min, G × R decreased mainly due to the decrease of G and the grain size slightly increased because of the decrease of G × R. This study combining numerical modeling and experimental researches reveals the relationship between processing parameters and grain size of laser metal deposition and the underlying mechanisms. It is reasonable to expect that this study will contribute to the microstructure and properties control of additive manufacturing.

Acknowledgement

This work was supported by the National Natural Science Foundation of China under grant Nos. 11502269 and 11672304.

Appendix A. Supplementary material

Supplementary data to this article can be found online at https://doi.org/10.1016/j.optlastec.2019.105662.

References

[1] N. Li, S. Huang, G. Zhang, R. Qin, W. Liu, H. Xiong, G. Shi, J. Blackburn, Progress in additive manufacturing on new materials: a review, J. Mater. Sci. Technol. 35 (2019) 242–269.
[2] D. Gu, Materials creation adds new dimensions to 3D printing, Sci. Bull. 61 (2016) 1718–1722.
[3] D.D. Gu, W. Meiners, K. Wissenbach, R. Poprawe, Laser additive manufacturing of metallic components: materials, processes and mechanisms, Int. Mater. Rev. 57 (2012) 133–164.
[4] S.A. David, T. Debroy, Current issuses and problems in welding science, Science 257 (1992) 497–502.
[5] T. DebRoy, H.L. Wei, J.S. Zuback, T. Mukherjee, J.W. Elmer, J.O. Milewski, A.M. Beese, A. Wilson-Heid, A. De, W. Zhang, Additive manufacturing of metallic components – Process, structure and properties, Prog. Mater. Sci. 92 (2018) 112–224.
[6] W. Ya, B. Pathiraj, S. Liu, 2D modelling of clad geometry and resulting thermal cycles during laser cladding, J. Mater. Process. Technol. 230 (2016) 217–232.
[7] H. El Cheikh, B. Courant, S. Branchu, J.-Y. Hascoet, R. Guillen, Analysis and prediction of single laser tracks geometrical characteristics in coaxial laser cladding process, Opt. Lasers Eng. 50 (2012) 413–422.
[8] P. Nie, O.A. Ojo, Z. Li, Modeling analysis of laser cladding of a nickel-based superalloy, Surf. Coat. Technol. 258 (2014) 1048–1059.
[9] R. Parekh, R.K. Buddu, R.I. Patel, Multiphysics simulation of laser cladding process to study the effect of process parameters on clad geometry, 3rd International Conference on Innovations in Automation and Mechatronics Engineering 2016, 2016, pp. 529–536.
[10] H. Qi, J. Mazumder, H. Ki, Numerical simulation of heat transfer and fluid flow in coaxial laser cladding process for direct metal deposition, J. Appl. Phys. 100 (2006).
[11] X. He, J. Mazumder, Transport phenomena during direct metal deposition, J. Appl. Phys. 101 (2007).
[12] W. Gao, S. Zhao, Y. Wang, Z. Zhang, F. Liu, X. Lin, Numerical simulation of thermal field and Fe-based coating doped Ti, Int. J. Heat Mass Transf. 92 (2016) 83–90.
[13] A. Emamian, M. Alimardani, A. Khajepour, Correlation between temperature distribution and in situ formed microstructure of Fe-TiC deposited on carbon steel using laser cladding, Appl. Surf. Sci. 258 (2012) 9025–9031.
[14] Z. Gan, G. Yu, X. He, S. Li, Numerical simulation of thermal behavior and multicomponent mass transfer in direct laser deposition of Co-base alloy on steel, Int. J. Heat Mass Transf. 104 (2017) 28–38.
[15] A. Kumar, S. Roy, Effect of three-dimensional melt pool convection on process characteristics during laser cladding, Comput. Mater. Sci. 46 (2009) 495–506.
[16] S. Li, H. Xiao, K. Liu, W. Xiao, Y. Li, X. Han, J. Mazumder, L. Song, Melt-pool motion, temperature variation and dendritic morphology of Inconel 718 during pulsed-and continuous-wave laser additive manufacturing: a comparative study, Mater. Des. 119 (2017) 351–360.
[17] J. Song, Y. Chew, G. Bi, X. Yao, B. Zhang, J. Bai, S.K. Moon, Numerical and experimental study of laser aided additive manufacturing for melt-pool profile and grain orientation analysis, Mater. Des. 137 (2018) 286–297.
[18] N. Raghavan, R. Dehoff, S. Pannala, S. Simunovic, M. Kirka, J. Turner, N. Carlson, S.S. Babu, Numerical modeling of heat-transfer and the influence of process parameters on tailoring the grain morphology of IN718 in electron beam additive manufacturing, Acta Mater. 112 (2016) 303–314.
[19] Y. Lian, Z. Gan, C. Yu, D. Kats, W.K. Liu, G.J. Wagner, A cellular automaton finite volume method for microstructure evolution during additive manufacturing, Mater. Des. 169 (2019).
[20] S.J. Wolff, Z. Gan, S. Lin, J.L. Bennett, W. Yan, G. Hyatt, K.F. Ehmann, G.J. Wagner, W.K. Liu, J. Cao, Experimentally validated predictions of thermal history and microhardness in laser-deposited Inconel 718 on carbon steel, Addit. Manuf. 27 (2019) 540–551.
[21] N.A. Kistler, A.R. Nassar, E.W. Reutzel, D.J. Corbin, A.M. Beese, Effect of directed energy deposition processing parameters on laser deposited Inconel (R) 718: microstructure, fusion zone morphology, and hardness, J. Laser Appl. 29 (2017).
[22] H.Y. Wan, Z.J. Zhou, C.P. Li, G.F. Chen, G.P. Zhang, Effect of scanning strategy on grain structure and crystallographic texture of Inconel 718 processed by selective laser melting, J. Mater. Sci. Technol. 34 (2018) 1799–1804.
[23] K. Yuan, W. Guo, P. Li, J. Wang, Y. Su, X. Lin, Y. Li, Influence of process parameters and heat treatments on the microstructures and dynamic mechanical behaviors of Inconel 718 superalloy manufactured by laser metal deposition, Mater. Sci. Eng. A-

Struct. Mater. Propert. Microstruct. Process. 721 (2018) 215–225.
[24] F. Caiazzo, Laser-aided directed metal deposition of Ni-based superalloy powder, Opt. Laser Technol. 103 (2018) 193–198.
[25] A.D. Brent, V.R. Voller, K.J. Reid, Enthalpy-porosity technique modeling convection-diffusion phase-change – application to the melting of a pure metal, Numer. Heat Transf. 13 (1988) 297–318.
[26] D.R. Poirier, Permeability for flow of interdendritic liquid in columnar-dendritic alloys, Metall. Trans. B-Process Metall. 18 (1987) 245–255.
[27] A. Kar, J. Mazumder, Model for nonequilibrium partitioning during rapid solidification of binary concentrated-solutions, Acta Metall. Mater. 40 (1992) 1873–1881.
[28] R.K.C. Chan, Generalized aebitrary Lagrangian-Eulerian method for incompressible flows with sharp interfaces, J. Comput. Phys. 17 (1975) 311–331.
[29] S. Morville, M. Carin, P. Peyre, M. Gharbi, D. Carron, P. Le Masson, R. Fabbro, 2D longitudinal modeling of heat transfer and fluid flow during multilayered direct laser metal deposition process, J. Laser Appl. 24 (2012).
[30] M.J. McNallan, T. Debroy, Effect of temperature and composition on surface-tension in Fe-Ni-Cr alloys containing sulfur, Metall. Trans. B-Process Metall. 22 (1991) 557–560.
[31] S. Kou, Welding Metallurgy, second ed., John Wiley & Sons, Hoboken, NJ, 2003.
[32] C. Saintecatherine, M. Jeandin, D. Kechemair, J.P. Ricaud, L. Sabatier, Study of dynamic absorptivity at 10.6μm (CO2) and 1.06μm (Nd:YAG) wavelengths as a function of temperature, J. Phys. IV 1 (1991) 151–157.
[33] X. He, L. Song, G. Yu, J. Mazumder, Solute transport and composition profile during direct metal deposition with coaxial powder injection, Appl. Surf. Sci. 258 (2011) 898–907.
[34] K.C. Mills, Recommended Values of Thermophysical Properties for Selected Commercial Alloys, Woodhead Publishing, 2002.
[35] P. Sahoo, T. Debroy, M.J. McNallan, Surface-tension of binary metal – surface-active solute systems under conditions relevant to welding metallurgy, Metall. Trans. B-Process Metall. 19 (1988) 483–491.
[36] Y.S. Li, Y. Niu, G.Y. Fu, W.T. Wu, F. Gesmundo, Effect of grain size reduction on high temperature oxidation of binary two-phase alloys, Trans. Nonferr. Met. Soc. China 11 (2001) 644–648.
[37] T.G. Langdon, Grain boundary sliding revisited: developments in sliding over four decades, J. Mater. Sci. 41 (2006) 597–609.
[38] M.C. Flemings, Solidification Processing, Wiley Online Library, 1974.